

## Article

# Zonal Geochemistry and Elasticity Characteristics of Gallium- and Lithium-Rich No. 6 Coalbed in the Haerwusu Mine, North China

Jiannan Fu <sup>1</sup> , Tongjun Chen <sup>2,\*</sup>  and Fan Cui <sup>1</sup>

<sup>1</sup> College of Geoscience and Survey Engineering, China University of Mining and Technology (Beijing), Beijing 100083, China; fujiannan5899@163.com (J.F.); cuifan@cumtb.edu.cn (F.C.)

<sup>2</sup> School of Resource and Earth Science, China University of Mining and Technology, Xuzhou 221116, China

\* Correspondence: tjchen@cumt.edu.cn

**Abstract:** This paper presents the zonal geochemistry and elasticity characteristics of gallium- and lithium-rich No. 6 coalbed in the Haerwusu mine and discusses interpretation methodologies of coal-hosted gallium and lithium resources using lab-measured samples and field-measured wireline logs. The results demonstrate that both coal-composition-based and elastic-parameter-based classifications yield similar results, categorizing the coalbed into subzones related to coal quality. Material compositions, elastic properties, critical metals, and host minerals exhibit zonal distribution characteristics within the ultrathick No. 6 coalbed. Three-class classifications significantly enhance correlations among host minerals, elastic parameters, and critical metals, albeit with differing trends among classes. In classes II and III (ultralow- and low-ash-yield coals), boehmite and kaolinite primarily host gallium and lithium, respectively. In class I (medium-ash-yield coal), gallium is associated with kaolinite, while lithium lacks specific mineral associations. Constrained by wireline logs, a rock physics modeling strategy is proposed to link mesoscale coal compositions to macroscale elastic responses. Moreover, explicit correlations between host minerals and critical metals are established, connecting macroscale elastic responses to microscale gallium and lithium enrichments and exploring interpretation methods of coal-hosted critical metals. Preferred lithium interpretation methods include compositional ternary plots and elastic parameter cross plots, while preferred gallium interpretation methods involve boehmite-gallium and elastic parameter-gallium fitting. These findings may contribute to understanding the enrichment mechanisms and interpretation technologies of coal-hosted critical metals in ultrathick low-rank coalbeds.

**Keywords:** ultrathick coalbed; critical metal; zonal characteristic; rock physics modeling; petrophysical parameter; interpretation



**Citation:** Fu, J.; Chen, T.; Cui, F. Zonal Geochemistry and Elasticity Characteristics of Gallium- and Lithium-Rich No. 6 Coalbed in the Haerwusu Mine, North China. *Minerals* **2024**, *14*, 404. <https://doi.org/10.3390/min14040404>

Academic Editor: Thomas Gentzis

Received: 14 February 2024

Revised: 8 April 2024

Accepted: 11 April 2024

Published: 15 April 2024



**Copyright:** © 2024 by the authors. Licensee MDPI, Basel, Switzerland. This article is an open access article distributed under the terms and conditions of the Creative Commons Attribution (CC BY) license (<https://creativecommons.org/licenses/by/4.0/>).

## 1. Introduction

Gallium serves as a critical element in modern electronics and semiconductors, while lithium plays a vital role in addressing global climate changes [1,2]. Both metals are critical for contemporary industries. With the rapid development of semiconductor technology and the increasing demand for lithium batteries, there is a growing need for gallium and lithium resources to bridge the supply–demand gap [3]. Recent studies have identified gallium- and lithium-rich deposits within Permian–Carboniferous coalbeds in North China, encompassing regions such as Inner Mongolia’s Jungar coalfield and Shanxi province’s Qinshui and Ningwu coalfields [4–8]. Given the generally substantial and stable nature of coal seams in North China, coal-bearing formations in the region have the potential to host significant deposits of gallium and lithium.

Gallium and lithium enrichments within coal-bearing strata are influenced by a multitude of geological and geochemical factors, including the types of plants involved in coal formation, sediment sources, hydrothermal and groundwater processes, magmatic and

volcanic activities, seawater intrusions, and various depositional environments [5,9,10]. In Permian–Carboniferous coal seams of North China, gallium is primarily associated with diverse minerals, with boehmite and kaolinite being predominant, while lithium is commonly found in aluminosilicate minerals such as kaolinite, illite, chlorite, and boehmite [7,11,12]. However, the distribution of gallium and lithium within coalbeds is heterogeneous. Due to constraints of workloads and economic feasibility, conventional geochemical analyses often struggle to fully characterize the three-dimensional distribution of gallium- and lithium-rich ores in coalbeds. Previous studies have identified the ultrathick No. 6 coalbed in the Jungar coalfield as possessing significant gallium and lithium resources, elucidating their primary host minerals and sedimentary sources. However, the zonal characteristics, encompassing mineral compositions, host minerals, and elastic properties, remain largely underexplored.

Although wireline logging is an indirect exploration method, it boasts higher survey efficiency and sampling density compared to geochemical analyses [13]. In theory, it can provide a higher-resolution characterization of geological anomalies than geochemical methods, provided there is a correlation between geological formations and measured petrophysical and elastic parameters [13–15]. Wireline logs have been extensively utilized in coal, oil, gas, and traditional metal mining industries for exploring and delineating geological formations of interest [13–18]. In the context of coal-bearing metal deposits, a study by [19] utilized Gamma-ray logs to measure the thickness of uranium-rich deposits in coalbeds in Xinjiang. However, practical applications employing wireline logs to characterize gallium- and lithium-rich deposits in coalbeds are scarce.

Like wireline logging, rock physics modeling is valuable for delineating correlations among elastic parameters and geological targets. Researchers have applied rock physics modeling extensively in the oil and gas industry to understand the petrophysical and elastic characteristics of various formations such as sandstone, shale, carbonate, and unconventional reservoirs [20–23]. The elastic parameters commonly discussed include bulk and shear moduli, P- and S-wave impedances and velocities, quality factor Q, Poisson's ratio, and anisotropy parameters. In the coal industry, pioneers have utilized rock physics modeling to delineate coal-rank-related velocities and anisotropies, bulk moduli associated with absorbed methane, and variations in velocities and moduli related to gallium content [24–27]. Additionally, rock physics modeling has been employed to construct interpretation templates for oil and gas reservoirs as well as coal-hosted gallium deposits [24,28–30]. However, there have been few applications of rock physics modeling to uncover the zonal characteristics of elasticities and interpretation methodologies for coal-hosted gallium and lithium deposits in ultrathick coalbeds.

This paper utilizes the No. 6 coalbed in the Haerwusu mine as a case study to uncover the zonal characteristics of mineral compositions, elasticities, host minerals, and critical metals. Furthermore, it discusses the interpretation methods for gallium and lithium resources in the ultrathick No. 6 coalbed.

## 2. Geological Setting and Core Sampling

### 2.1. Geological Setting

The Haerwusu mine stands as a significant producer within the Jungar coalfield, situated on the northeast margin of the Ordos basin in North China (see Figure 1). With a mining area spanning 61.4 km<sup>2</sup> and a coal reserve estimated at 1.73 billion tons, it holds substantial importance [4,24]. The primary coal-bearing formations in the mine consist of the Carboniferous Taiyuan and lower Permian Shanxi formations. Notable minable coalbeds within the Taiyuan Formation include the No. 6 and No. 9 coalbeds, while the Shanxi Formation hosts the minable No. 5 coalbed. Among these, the No. 6 coalbed boasts the greatest thickness (~21 m), followed by the No. 9 coalbed (~4.1 m), and the thinnest, the No. 5 coalbed (~1.4 m). Remarkably, the No. 6 coalbed, characterized as long-flame coal ( $R_o \approx 0.57\%$ ), contributes to 80% of the recoverable coal reserve.

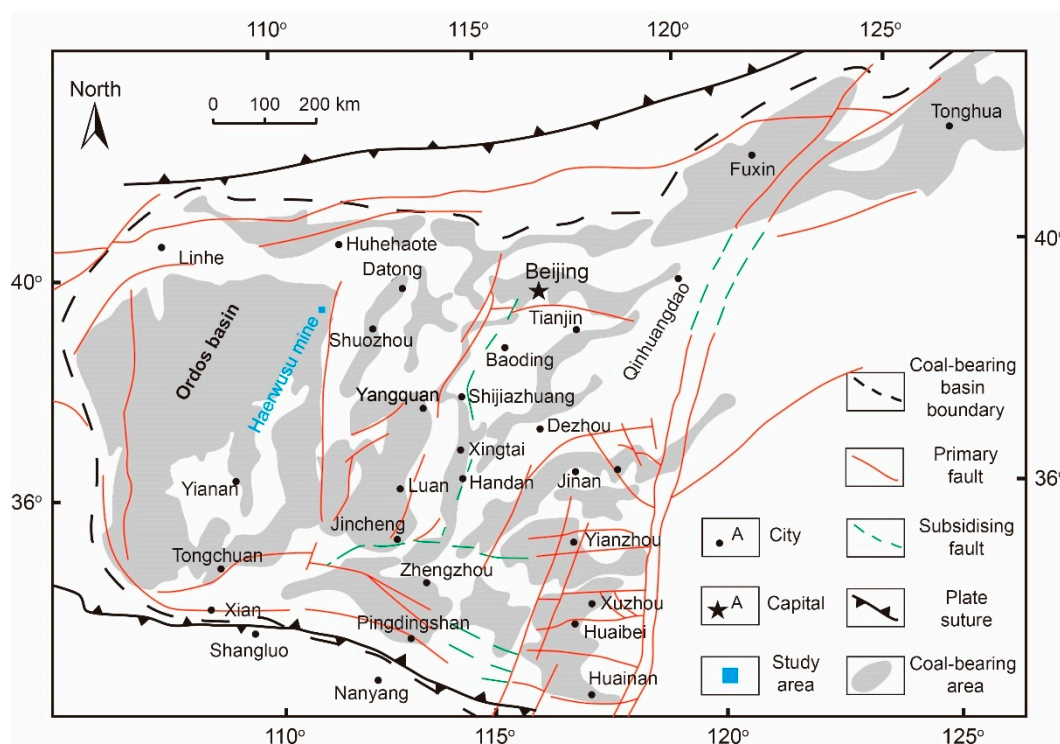


**Figure 1.** Coal-bearing basins in the Northern China plate and the Haerwusu mine location.

Along with the Jungar coalfield, the mine features relatively simple geological structures. Typically, it exhibits a monocline orientation, striking near the NS direction and dipping westward [4]. Consequently, its eastern portion comprises an uplifted terrace with an average depth of 80 m, while the western side forms a depression with an average depth of 100 m. Folds and faults within the mine are sparsely developed, primarily trending along the NE direction and existing on a small scale. Apart from areas near fold terminations and faults, sedimentary layers within the mine remain relatively flat, with dip angles generally less than 5°. However, near fold terminations and fault zones, dip angles can reach up to 20°.

## 2.2. Core Sampling and Testing

Recent research has revealed that the No. 6 coalbed in the Haerwusu mine boasts significant concentrations of gallium and lithium, with the weathered surface of the Benxi Formation in the north of the Ordos basin identified as the sedimentary provenance [4,6]. The rare earth elements present in the coalbed primarily originate from the bauxite of the Benxi Formation and overlying partings. Given the ultrathick nature of the No. 6 coalbed in the Haerwusu mine, it serves as an ideal site for investigating the zonal characteristics of mineral compositions and elasticities in ultrathick coalbeds. To facilitate this investigation, 29 coal samples were collected from drilling cores within the mine [4]. Figure 2 depicts the locations of these samples and their respective lithologies.

Geochemical measurements, including proximate analyses, inductively coupled plasma mass spectrometry (ICP-MS), and X-ray powder diffraction (XRD), were employed to analyze the No. 6 coalbed samples and understand the gallium and lithium contents, as well as compositional variation characteristics. Initially, the samples were crushed and ground into grains with sizes smaller than 200 mesh. Subsequently, proximate analyses were conducted following ASTM D3173-03, D3174-04, and D3175-02 standards. Following this, ICP-MS was utilized to measure the gallium and lithium contents of the samples. Finally, XRD was employed to estimate the major mineral contents.

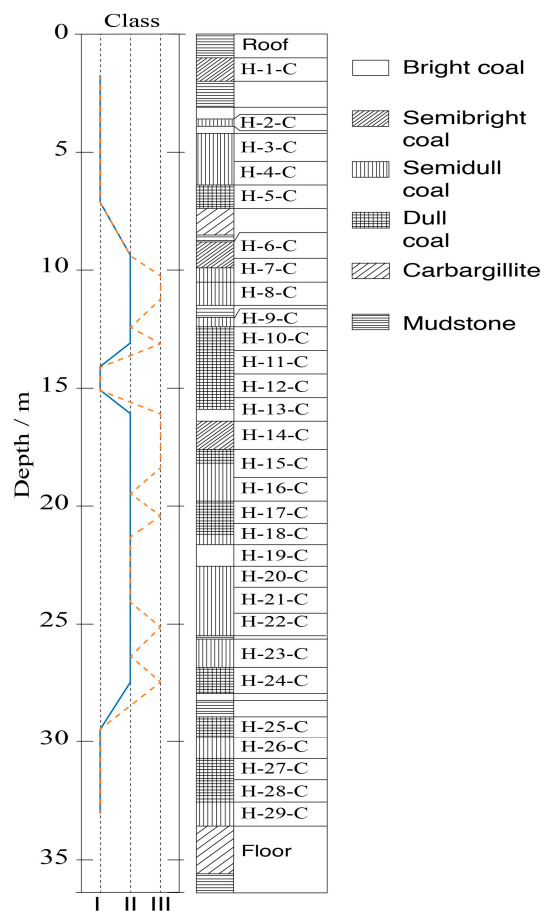


**Figure 2.** Comparison between lithological column, sample locations, and classified classes from coal compositions. The solid and dashed lines result from two- and three-class classifications.

### 2.3. Overall Geochemistry Characteristics

After completing the aforementioned procedures, the geochemistry results are compiled and plotted in Table 1 [4] and Figure 3. The gallium, lithium, organic, and mineral contents within the No. 6 coalbed exhibit significant heterogeneity. Coal benches proximate to the roof and floor of the coalbed typically display lower organic matter and higher kaolinite contents (medium-ash-yield) compared to those situated in the middle (ultralow- and low-ash-yield coals). Additionally, benches near the coalbed floor tend to exhibit relatively high levels of calcite, pyrite, and lithium. Meanwhile, boehmite and gallium contents are relatively elevated in benches located beneath the carbargillite parting (Figure 2). Given that the contents of kaolinite, calcite, pyrite, quartz, and boehmite are substantially higher than other minerals, this paper designates them as major minerals and utilizes them to analyze correlations. Notably, among all major minerals, kaolinite content predominates.

Pearson correlation coefficients have been used to quantify the relationship among organic matter, major minerals, gallium, and lithium. As depicted in Figure 4, most minerals and organic matter exhibit weak correlations, except for organic-kaolinite and calcite-pyrite pairs. The strong correlation between kaolinite and organic matter can be attributed to the significant contribution of kaolinite to the overall ash yield. Similarly, the strong correlation between pyrite and calcite can be explained by the association of most pyrite grains in coal with calcite veins. Regarding gallium and lithium, they exhibit weak to moderate correlations with minerals and organic matter, including boehmite and kaolinite. These findings suggest the complexity of gallium and lithium host minerals within the coalbed and raise doubts about conventional beliefs. Previously, it was thought that gallium and lithium were hosted by boehmite and kaolinite through element substitution and absorption [5,11,31–34].

**Table 1.** Measured gallium, lithium, organic matter, and mineral contents of coal samples from the No. 6 coalbed in the Haerwusu mine (vol%; on rock basis). Rt, Sd, and Class represent rutile, siderite, and three-class classification, respectively.

Sample	OM vol%	Kln vol%	Qtz vol%	Py vol%	Rt vol%	Cal vol%	Sd vol%	Bhm vol%	Ga µg/g	Li µg/g	Class
H-1-C	88.2	11.6	0.2	0	0	0	0	0	19	40	I
H-2-C	74.6	25.1	0.2	0	0.1	0	0	0	26	91	I
H-3-C	78	21	0.6	0	0	0.4	0	0	21	100	I
H-4-C	88	10	0.6	0.2	0.4	0.2	0	0.6	27	95	I
H-5-C	82.6	15.7	0	0.2	0.2	0	0	1.3	8.9	254	I
H-6-C	94.8	2	0.6	0	0.2	0.2	0	2.2	40	13	II
H-7-C	82	3	1.6	0.6	0.4	0	0	12.4	36	129	III
H-8-C	84.6	4.3	0.4	0.4	0.2	1.6	0	8.5	18	37	III
H-9-C	97.2	1.3	0.5	0.2	0	0	0	0.8	12	1.2	II
H-10-C	90.3	2.4	0.7	0.4	0	1.5	0	4.7	13	62	III
H-11-C	79.6	12.6	1.6	0.4	0	0.6	0	5.2	15	231	I
H-12-C	80.5	12.2	0.7	0.2	0	1.4	0	5	14	222	I
H-13-C	91.2	1.6	1.8	0.4	0.2	1.2	0	3.6	16	29	III
H-14-C	84.7	6	0.8	0.4	0	0.6	0.2	7.3	27	70	III
H-15-C	90.5	3.4	0.4	0.6	0	1.9	0.2	3	12	30	III
H-16-C	94.3	1.1	0.4	0.9	0	2	0	1.3	16	23	II
H-17-C	91.6	2.6	0.6	0.2	0	2.2	0	2.8	16	82	III
H-18-C	96.4	1.9	0.2	0.2	0	1	0	0.3	7.4	3.9	II
H-19-C	96.6	1	0.2	0	0	1	0	1.2	16	20	II
H-20-C	97	1	0.4	0.2	0	0.8	0	0.6	11	0.06	II
H-21-C	90.7	6.5	0.8	0	0	1	0	1	9.7	273	II
H-22-C	87.2	7.1	0.2	0.2	0	0.7	0	4.6	15	48	III
H-23-C	96.1	2.3	0.2	0	0	0.2	0	1.2	20	41	II
H-24-C	87.8	8.1	0	0.2	0	0.6	0	3.3	15	301	III
H-25-C	85.4	6.3	0	0.9	0	6	0	1.4	12	324	I
H-26-C	84.9	14.1	0	0.2	0	0.8	0	0	19	129	I
H-27-C	84.1	15.5	0	0.2	0	0.2	0	0	23	470	I
H-28-C	81.7	13.1	0	1.4	0	3.8	0	0	22	169	I
H-29-C	73	19	0	3.2	0	4.8	0	0	23	87	I

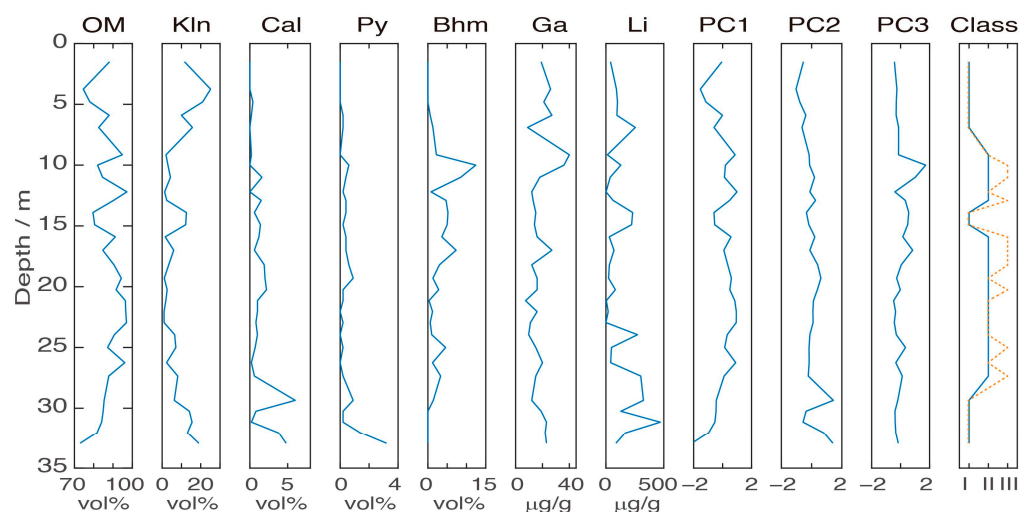


**Figure 3.** Tracks 1–5 represent the measured contents of organic matter and main minerals, while tracks 6 and 7 show the gallium and lithium contents. Tracks 8–11 correspond to the derived principal components (PC) and classified classes. The abbreviations OM, Kln, Cal, Py, Bhm, Ga, Li, PC1, PC2, PC3, and Class denote organic matter, kaolinite, calcite, pyrite, beohmite, gallium, lithium, principal component one, principal component two, principal component three, and classification, respectively. The solid and dashed lines result from two- and three-class classifications.

OM	1.00	-0.85	-0.21	-0.42	-0.14	-0.28	-0.43
Kln	-0.85	1.00	0.01	0.20	-0.33	0.17	0.43
Cal	-0.21	0.01	1.00	0.74	-0.13	-0.19	0.15
Py	-0.42	0.20	0.74	1.00	-0.04	0.09	0.02
Bhm	-0.14	-0.33	-0.13	-0.04	1.00	0.26	-0.05
Ga	-0.28	0.17	-0.19	0.09	0.26	1.00	-0.08
Li	-0.43	0.43	0.15	0.02	-0.05	-0.08	1.00
	OM	Kln	Cal	Py	Bhm	Ga	Li

**Figure 4.** Heatmap of Pearson correlation coefficients among organic matter, major minerals, gallium, and lithium for all samples from the No. 6 coalbed.

To examine the feasibility of conventional beliefs regarding the coalbed, we employed principal component analysis (PCA) to identify multiple correlations by plotting factor scores and loadings on the same diagram, as illustrated in Figure 5. Figure 5a exhibits the poles of lithium and kaolinite aligned, suggesting that kaolinite is the main trap mineral for lithium. The pole of gallium is situated between the poles of kaolinite and boehmite, implying that gallium is likely attributed to kaolinite and boehmite. Figure 5b displays that the poles of kaolinite and organic matter are distributed in near opposite directions, indicating that kaolinite is the primary ash yield of most samples. These phenomena are likely the interpretations of weak to moderate correlations among gallium, lithium, major minerals, and organic matter. Therefore, the conventional beliefs on gallium and lithium trap minerals in the coalbed are still valid, but in a more complex form.

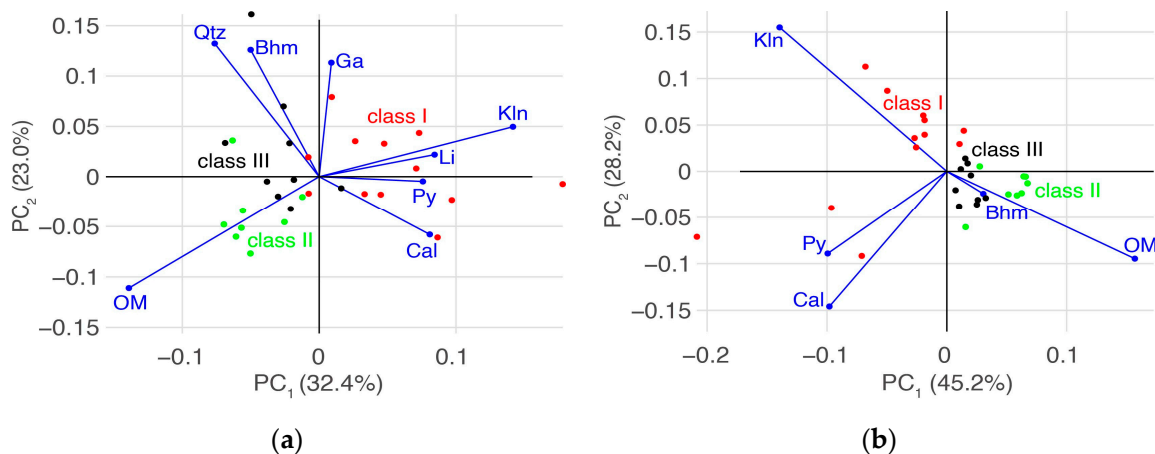


**Figure 5.** PCA with minerals, gallium, and lithium across various coal types (a), and PCA on minerals only displaying different types of coals characterized by their OM content, as opposed to kaolinite, with some samples enriched in pyrite and calcite (b).

### 3. Zonal Geochemistry Characteristics

#### 3.1. Classification Methodology

The weak to moderate correlations observed between rare metals (gallium and lithium) and minerals hinder the exploration of gallium and lithium resources in the coalbed. Given that the No. 6 coalbed exhibits ultrathick characteristics and displays vertical heterogeneities in compositions, there is a desire to classify the ultrathick coalbed into distinct subzones. This classification aims to refine the correlations between rare metals

and minerals. The input for this classification consists of sample compositions, specifically the volume contents of organic matter and major minerals.

Since coal compositions exhibit correlations in Figure 4, we begin by employing principal component analysis (PCA) to calculate the linearly uncorrelated principal components (PCs) of coal compositions. Subsequently, we utilize variance contributions to select the most favorable combinations of PCs [35]. Table 2 presents the coefficient matrix of the PCA analysis for all samples, where each column provides the coefficients of coal compositions for calculating the corresponding PC. Additionally, Table 3 presents the eigenvalues and variance contributions of the PCs. Considering that the first three PCs contribute to 96% of the variance, this study utilizes these first three PCs as input (refer to Figure 3) and employs k-means clustering to classify all samples [36]. By considering the compositional variation characteristics, this study gradually increases the number of classes from two to three and subsequently discusses the zonal geochemistry characteristics of each class.

**Table 2.** The coefficient matrix of PCA analysis for all samples.

Content	PC1	PC2	PC3	PC4	PC5
Organic	0.67	0.09	−0.33	0.10	0.65
Kaolinite	−0.66	−0.35	−0.18	−0.05	0.64
Calcite	−0.20	0.78	−0.08	−0.57	0.14
Pyrite	−0.26	0.52	0.04	0.81	0.09
Boehmite	0.11	0.01	0.92	−0.06	0.37

**Table 3.** The eigenvalues and variance contributions of PCs.

Content	Eigenvalues	Variance Contributions	Cumulative Contributions
PC1	0.62	0.50	0.50
PC 2	0.32	0.25	0.75
PC 3	0.27	0.21	0.96
PC 4	0.04	0.04	1.00
PC5	0.00	0.00	1.00

### 3.2. Zonal Geochemistry Characteristics after Two-Class Classification

Following the procedures outlined in Section 3.1, we classify all samples into two classes and present the results in the last track of Figure 3 (solid blue). In general, class I is primarily situated at the top and bottom of the coalbed, while class II is located in the middle. In comparison to the proximate analysis results, class I corresponds to medium-ash-yield coal, whereas class II corresponds to ultralow- and low-ash-yield coals.

Like Section 2.3, we compute the Pearson correlation coefficients of classes I and II and present the results in Figure 6. As depicted, the two-class classification noticeably improves the correlations of gallium-boehmite and lithium-kaolinite pairs, although the improvements vary between classes. In class I, gallium positively correlates with kaolinite ( $R = 0.42$ ) rather than boehmite ( $R = -0.55$ ), whereas in class II, gallium positively correlates with boehmite ( $R = 0.55$ ) rather than kaolinite ( $R = -0.01$ ). Hence, the host minerals of gallium differ between classes I and II. Similarly, lithium in class II positively correlates with kaolinite but weakly correlates with all minerals in class I. Additionally, organic matter in both classes exhibits limited affinity for hosting lithium. Consequently, the hosts of gallium and lithium in the coalbed exhibit complexity, as previously suggested by references [11,31], and display zonal characteristics.

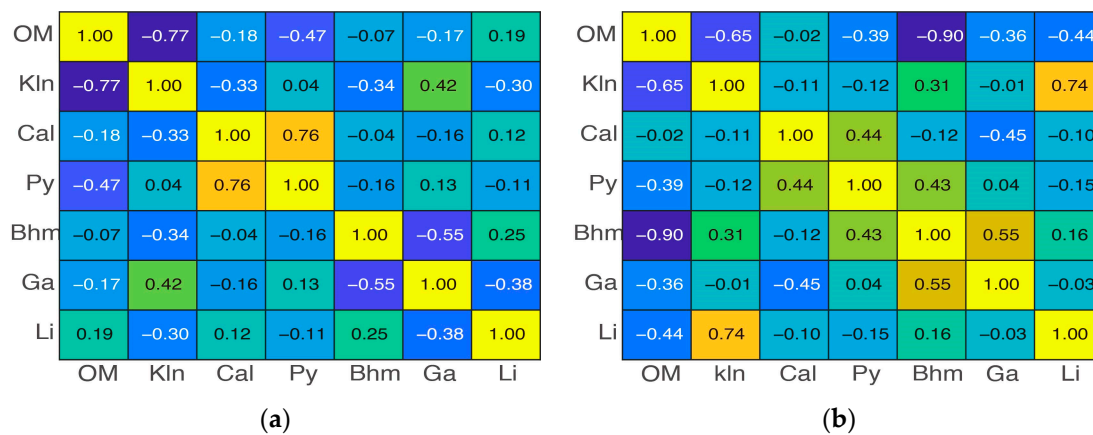


Figure 6. Heatmaps of Pearson correlation coefficients among gallium, lithium, organic matter, and main minerals for classes I (a) and II (b) after two-class classification.

3.3. Zonal Geochemistry Characteristics after Three-Class Classification

As illustrated in Section 3.2, we classify all samples into three classes and present the results in the last track of Figure 3 (dash yellow). Class I remains consistent in both two- and three-class classifications, primarily situated at the top and bottom of the coalbed. Classes II and III are located in the middle of the coalbed and exhibit periodic gyration characteristics. In comparison to the proximate analysis results, class II corresponds to ultralow-ash-yield coal, while class III corresponds to low-ash-yield coal. Moreover, calcite-pyrite pairs display a high correlation in class II but a weak correlation in class III. These zonal phenomena may be linked to the micro variations in the sedimentary environment during coal formations.

As class I remains consistent in both classifications, we solely compute the Pearson correlation coefficients of classes II and III and compare them in Figure 7. Generally, classes II and III exhibit similar correlation patterns but differ in the specific correlation coefficients. The correlation coefficients of the gallium-boehmite pair in classes II and III and the lithium-kaolinite pair in class II are high ( $R = 0.93, 0.88,$  and  $0.97,$  respectively). In contrast, the correlation coefficient of the lithium-kaolinite pair in class III is moderate ( $R = 0.56$ ), while the correlation coefficient of the lithium-kaolinite pair in class I is low ( $R = -0.3$ ). Compared to the two-class classification, the three-class classification significantly enhances correlation coefficients among the mentioned pairs. Moreover, organic matter demonstrates a strong negative correlation with gallium in class III and lithium in class II. This phenomenon is likely due to the presence of organic matter, which tends to coincide with lower levels of kaolinite, thereby inducing negative correlations within the groups.

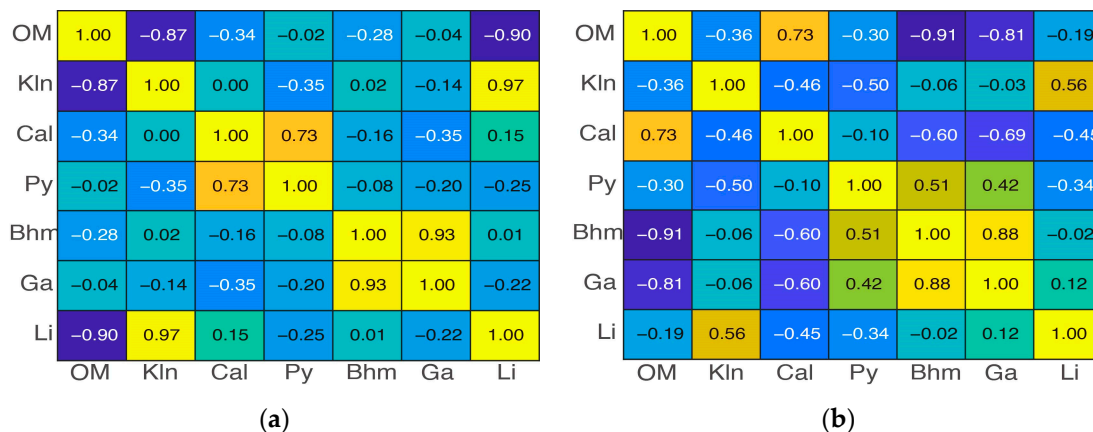
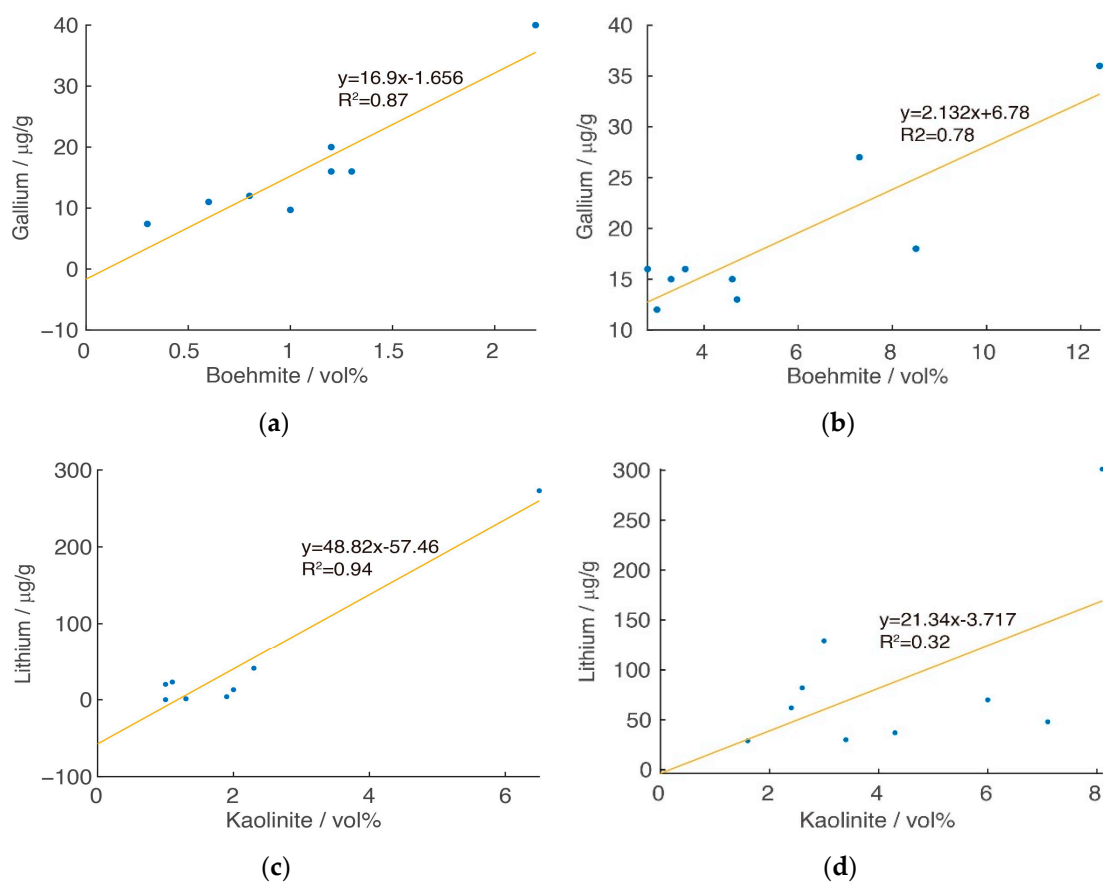


Figure 7. The heatmaps of Pearson correlation coefficients among gallium, lithium, organic matter, and minerals for classes II (a) and III (b) after three-class classification.

As the reliability of the Pearson correlation coefficient in evaluating cross-correlations in geochemistry is not always guaranteed [37,38], we have cross-plotted the gallium-boehmite and lithium-kaolinite pairs and fitted their variation trends in Figure 8. The results indicate that the calculated correlation coefficients are consistent with the cross plots. One can estimate the gallium and lithium contents using the fitted trends, except for lithium in class III (Figure 8d). Figure 8d illustrates the presence of two classes of kaolinites with a high correlation coefficient when separated: (i) the Li-enriched kaolinite (up to Li = 301 ppm) with aligned points in the upper part of the plot, and (ii) the Li-depleted kaolinite (maximum Li = 70 ppm) in the lower part. Both populations exhibit high correlation coefficients (0.98 and 0.75, respectively) with the kaolinite (vol%). Because it is hard to separate these two classes with the major minerals, we do not fit trends for them to interpret metal contents. Furthermore, the trend gradients and boehmite contents in Figure 8a,b vary significantly, suggesting that unit boehmite in class II has absorbed much more gallium than in class III. Exploring the reasons behind this intriguing phenomenon warrants research in the future.



**Figure 8.** The cross plots of boehmite vs. gallium (a,b) and kaolinite vs. lithium (c,d) for classes II (a,c) and III (b,d).

#### 4. Zonal Elasticity Characteristics

##### 4.1. Rock Physics Modeling Strategy

Generally, acoustic elasticities represent macroscale responses of subsurface samples and cannot directly relate to microscale metal enrichments. This section proposes a mesoscale rock physics modeling strategy to bridge the scale differences. Following Section 2.2, the strategy begins with coal compositions and follows the procedures outlined in Figure 9 [24,29,30]. As revealed by coal petrology, the occurrence states of minerals in No. 6 coalbed primarily consist of block- or plate-shaped grains floating in the organic matter [4,39]. Therefore, the strategy treats the organic matter as the background phase and

the minority minerals and pores as the inclusion phases. Given the 29 samples, the strategy deals with each sample separately.

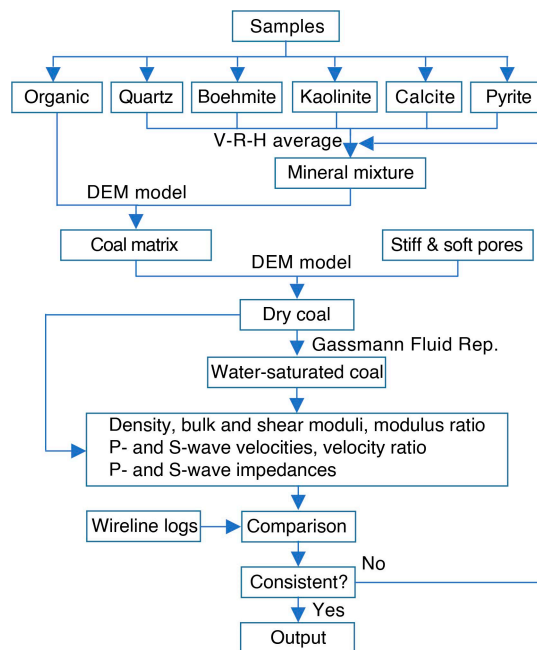


**Figure 9.** Rock physics modeling strategy for the gallium- and lithium-rich coal in the No. 6 coalbed.

For each sample, the strategy initially inputs its mineral fractions (Table 1) and physical parameters (Table 4) to compute the effective moduli of mineral mixtures using the V-R-H average (see Appendix A). Subsequently, the strategy incorporates the mineral mixture into the organic matter background to calculate the effective moduli of coal matrices using the DEM model (see Appendix B). Thirdly, the strategy progressively embeds stiff and soft pores (in the dry state) into coal matrices to determine the effective moduli of dry coal using the DEM model. The porosity considered here corresponds to the average of the No. 6 coalbed in the Haerwusu mine (9.4%). Fourthly, the strategy replaces dry pores with saturated water following the Gassmann fluid replacement strategy (see Appendix C). Finally, the strategy computes the elastic parameters of water-saturated coal according to isotropic linear elasticity theory (see Appendix D) and compares these parameters with measured wireline logs. If the modeled and wireline-logged parameters align, the results are outputted. If not, the strategy adjusts modeling parameters and repeats the rock physics modeling procedures starting from the step of mineral mixing.

**Table 4.** Moduli and densities of coal components have been used for rock physics modeling [40,41].

	Density (g/cc)	Bulk Modulus (GPa)	Shear Modulus (GPa)
Kaolinite	2.44	44	22
Quartz	2.65	37	44
Pyrite	4.93	147.4	132.5
Calcite	2.71	76.8	32
Boehmite	3.04	87.5	64.03
Organic	1.30	2.9	2.7

#### 4.2. Overall Elasticity Characteristics

After performing the rock physics modeling, we plot calculated elastic parameters, including bulk and shear moduli ( $K$  and  $\mu$ ), P- and S-wave velocities ( $V_P$  and  $V_S$ ), modulus and velocity ratios ( $K/\mu$  and  $V_P/V_S$ ), and densities (Den) in Figure 10. Generally, elastic parameters in tracks 1–7 exhibit similar variation trends. The values are higher near the

coalbed's roof and floor than in other locations. Elastic parameters in the water-saturated state are generally larger than in the dry state, except for S-wave velocity. Compared to the geochemistry results in Figure 3, the elastic parameters are positively correlated with kaolinite and negatively correlated with organic matter. Additionally, in comparison to gallium and lithium contents, high gallium contents are associated with low elastic parameters, while high lithium contents are associated with high elastic parameters.

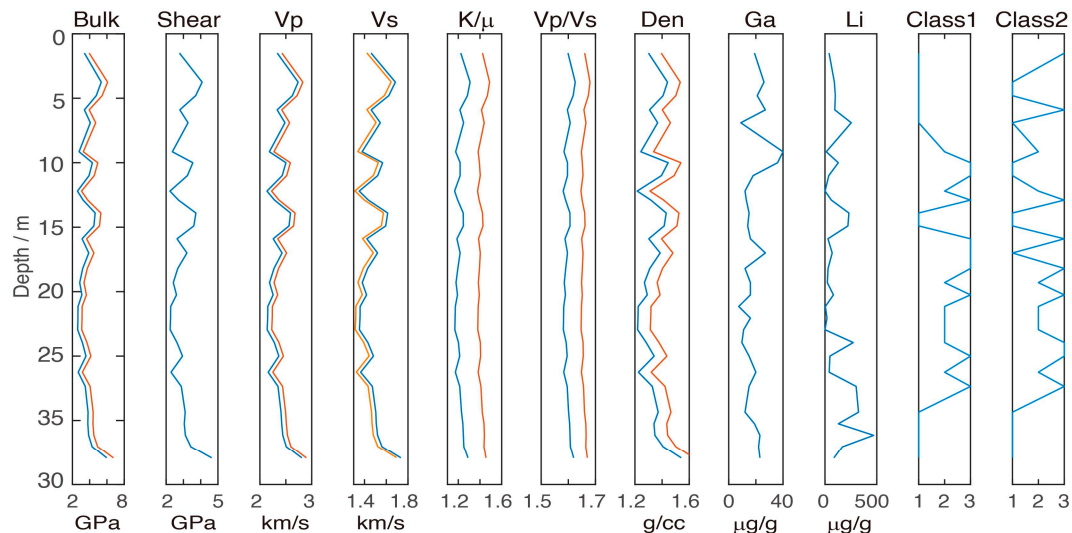


**Figure 10.** Tracks 1–7 represent calculated elastic parameters, tracks 8 and 9 denote gallium and lithium contents, and tracks 10 and 11 indicate classified classes based on coal compositions and elastic parameters. In tracks 1–7, the blue curves represent dry-state logs, and the orange curves represent water-saturated logs.

#### 4.3. Rock Physics Modeling Validation

To assess the feasibility of the proposed rock physics modeling strategy, we compare the modeled density and P-wave velocity with measured wireline logs from borehole C14 in the Haerwusu mine (see Figure 11). In comparison to the roof sandstone and floor mudstone, the No. 6 coalbed exhibits characteristics such as low density, low P-wave velocity ( $V_P$ ), low Gamma ray (GR), high resistivity (RD), high spontaneous potential (SP), and high caliper (CAL) [42]. The rapid and violent fluctuations observed in density,  $V_P$ , GR, and RD logs within the No. 6 coalbed suggest complex lithological and compositional variations.

Because the borehole is filled with drilling fluid (freshwater) during wireline logging, we approximate that the wireline logs were measured under a water-saturated state. In this comparison, this paper focuses solely on density and  $V_P$  parameters, as both wireline logs and rock physics modeling results have them. Due to differences in sampled benches and wireline logs in terms of locations and sample rates, their density and  $V_P$  values cannot be directly compared from sample to sample. Instead, both data sets should exhibit similar statistical characteristics, as their field locations are close together and share similar lithological and bedding characteristics. Therefore, this paper compares the probability distributions of modeled and wireline-logged density and  $V_P$  in Figure 12.

Because the wireline logs include data from roof sandstone, floor mudstone, and coalbed partings, the density and  $V_P$  variation ranges of wireline logs are larger than those of the rock physics modeling results. Fortunately, coal benches exhibit the lowest density and  $V_P$  within the No. 6 coalbed. Therefore, it suffices to compare the characteristics of the lower ends in Figure 12. Since the modeled and wireline-logged histograms are almost overlapped in the lower ends, these high consistencies can mutually verify the feasibility of the proposed modeling strategy in Section 4.1 and the reliability of sample measurements in Section 2.2. One can utilize the modeled elastic parameters to further discuss the geophysical interpretation technologies of gallium and lithium contents.

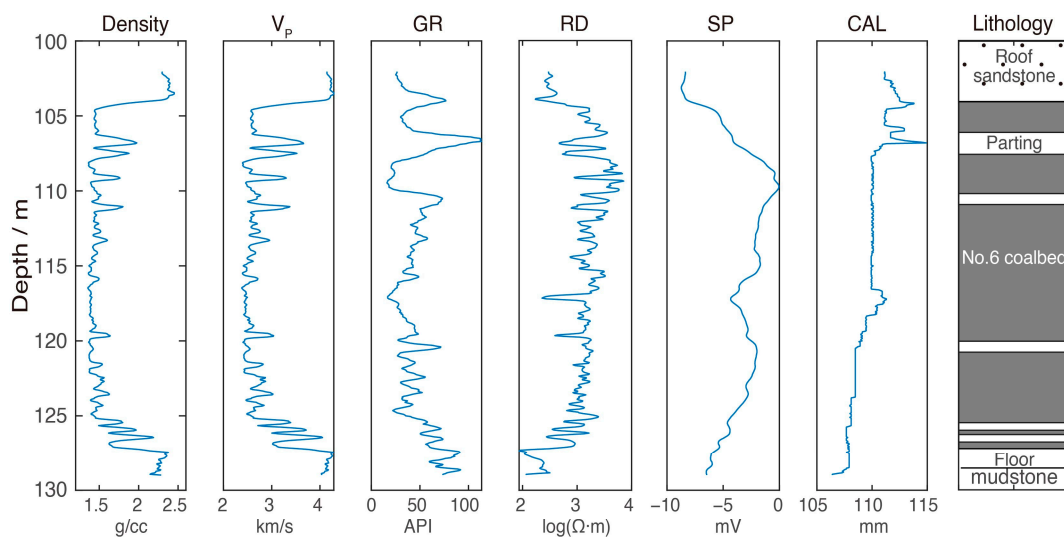


**Figure 11.** Measured wireline logs of borehole C14 under a water-saturated state around the No. 6 coalbed in the Haerwusu mine.

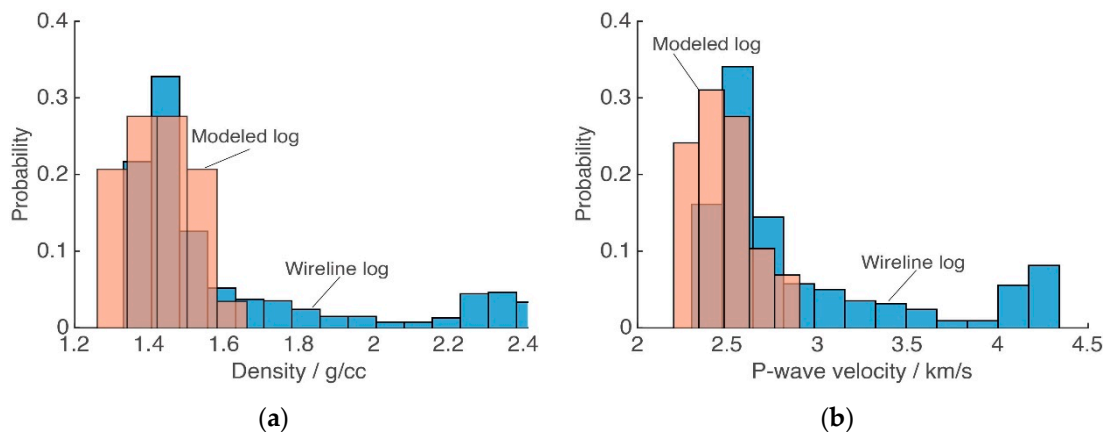


**Figure 12.** The probability distributions of modeled and wireline-measured density (a) and  $V_p$  (b) of the No. 6 coalbed in the Haerwusu mine.

#### 4.4. Zonal Elasticity Characteristics after Three-Class Classification

We utilize the rock physics modeled results to calculate Pearson correlation coefficients for all samples (see Figure 13a) and discuss the correlations among gallium, lithium, and elastic parameters. Generally, elastic parameters exhibit high correlations with each other, consistent with the wireline-logged results. In contrast, the correlations among gallium, lithium, and elastic parameters are generally low to moderate. The highest correlation coefficient between lithium and elastic parameters is 0.45 (for modulus and velocity ratios), and the highest coefficient between gallium and elastic parameters is 0.29 (for density and shear modulus). These phenomena represent a fundamental limit to directly interpreting critical metals using elastic parameters.

To mitigate the impact of potential multiple correlations, we employ PCA to analyze the relationships among elastic parameters, gallium, and lithium by plotting the factor scores and factor loadings on the same diagram, as illustrated in Figure 14. The poles of velocity and modulus ratios are close to the pole of lithium, suggesting that these two ratios likely correlate with lithium content. The pole of gallium is far away from the other poles, indicating that few elastic parameters are associated with gallium content. These phenomena validate the results of Pearson correlation coefficients and highlight a fundamental limitation in directly interpreting critical metals using elastic parameters in the coalbed.

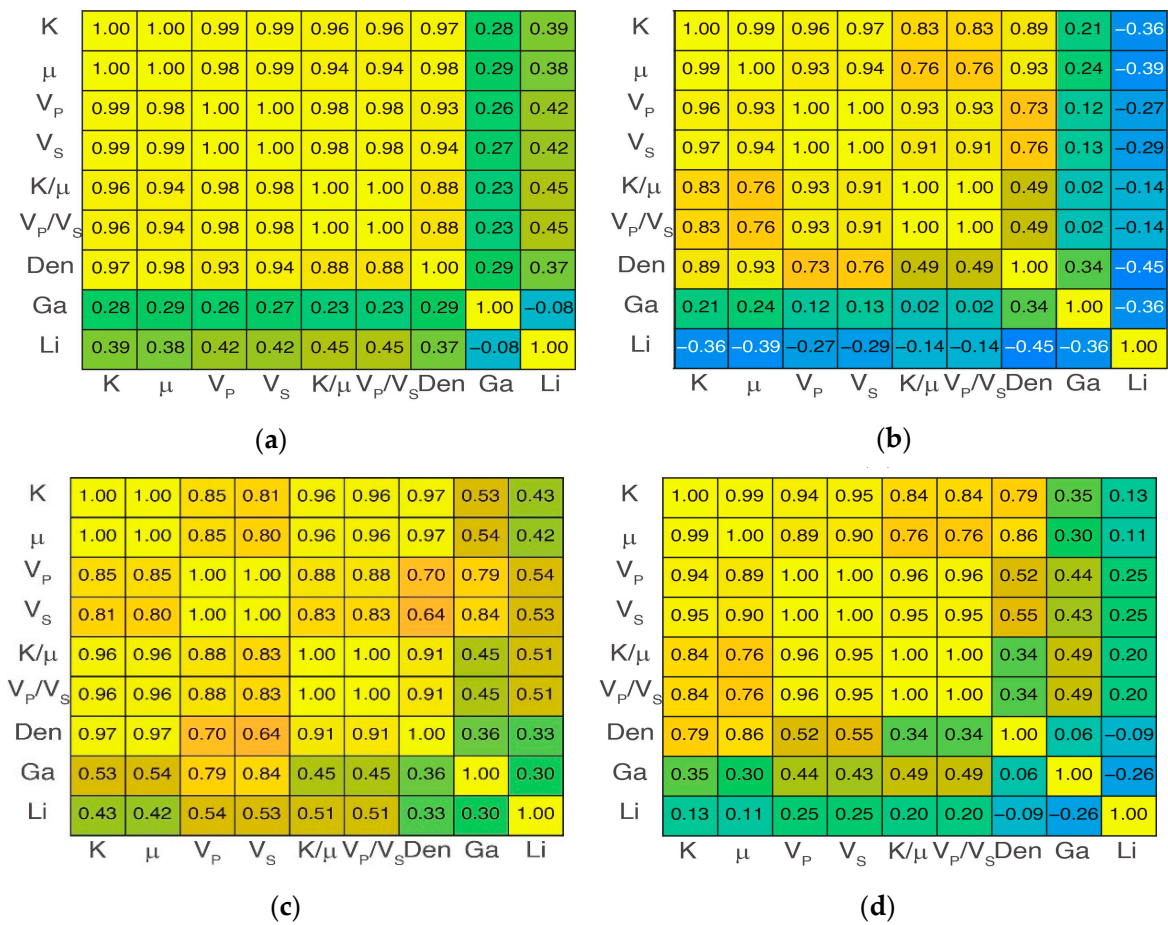


**Figure 13.** Heatmaps of Pearson correlation coefficients among elastic parameters, gallium, and lithium for the whole (a), class I (b), class II (c), and class III (d) benches.

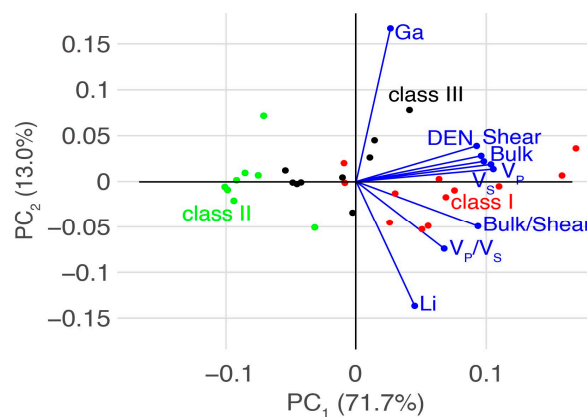


**Figure 14.** PCA with elastic parameters, gallium, and lithium with various coal types.

To enhance the correlation coefficients among elastic parameters, gallium, and lithium, we compute the PCs of all elastic parameters and utilize the first two PCs along with k-means clustering to classify all samples into three classes. The results are depicted in the last track of Figure 10. In comparison to the classified classes based on coal compositions (track 10), the classified classes derived from elastic parameters exhibit similar distributions. The consistency between these two classifications is high, at 79.3%. Classes I, II, and III correspond to high, low, and intermediate elastic values, respectively, and are roughly associated with medium-ash-yield, ultralow-ash-yield, and low-ash-yield benches.

The Pearson correlation coefficients among elastic parameters in Figure 13b–d generally exhibit similarities but differ from those in Figure 13a. Specifically, the coefficients between gallium and elastic parameters in Figure 13c,d are higher than those in Figure 13a, whereas the coefficients in Figure 13b are lower. Similarly, the coefficients between lithium and elastic parameters in Figure 13c are higher than in Figure 13a, whereas those in Figure 13b,d are lower. Notably, the highest correlation coefficient between lithium and elastic parameters is found in class II ( $V_P$ ,  $R = 0.54$ ), and the highest coefficient between gallium and elastic parameters is observed in class III (modulus and velocity ratios,  $R = 0.49$ ). Figure 10 indicates that class II exhibits the highest gallium content, while class I has the highest lithium content. In class II, the shear velocity ( $V_S$ ) shows the strongest correlation with gallium ( $R = 0.84$ ). As depicted in Figure 15a, gallium content can be confidently interpreted using the fitted trend. Conversely, in class I, density exhibits the strongest correlation with lithium ( $R = -0.45$ ). However, notable scatter deviations in the plot are evident, as illustrated in Figure 15b, raising questions about the reliability of interpreting lithium content using density fitting.

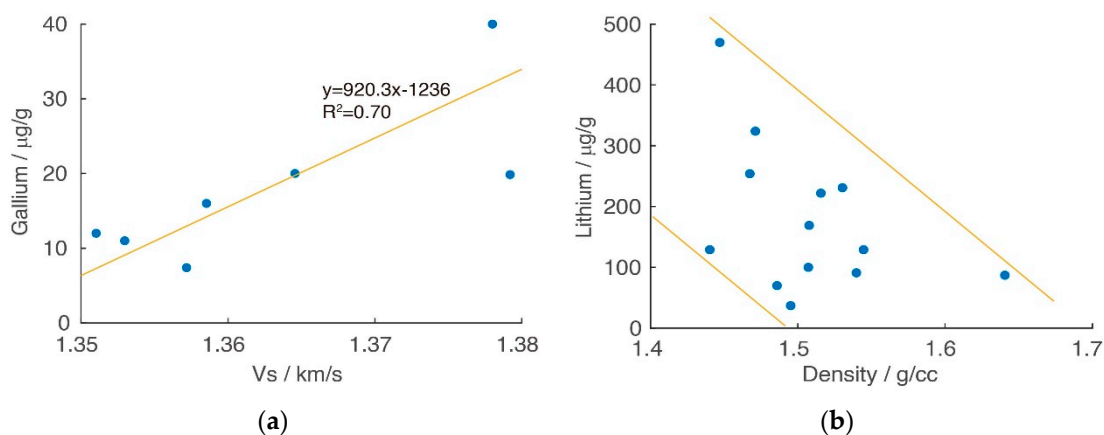


**Figure 15.** The cross plots of  $V_S$  vs. gallium for class II (a) and density vs. lithium for class I (b).

## 5. Discussion

### 5.1. Interpretation Method with Compositional Ternary Plot

The ternary plot serves as a valuable tool for distinguishing coal compositions and petrology. In this section, organic matter, kaolinite, and the sum of other minerals (mostly boehmite) are used as edges to construct the ternary plots, as depicted in Figure 16. The classified classes exhibit distinct zonal distribution characteristics, allowing for clear separation from each other. Similarly, lithium contents also demonstrate zonal distribution characteristics, with high-lithium samples primarily situated in the marked lithium-sweet zone (predominantly belonging to class I). Conversely, gallium contents lack zonal distribution characteristics, with high-gallium samples sparsely distributed across the ternary plot. This phenomenon is particularly pronounced in the subzone of class I compared to other subzones.

As previously discussed, coal compositions and correlations among critical metals and minerals in the coalbed exhibit zonal characteristics that are closely linked to sedimentary environments. These observations suggest that variations in sedimentary environment-related coal compositions influence the enrichments of gallium and lithium in the coalbed. High gallium contents are predominantly found in classes II and III, which can be effectively interpreted using boehmite-gallium fitting. Conversely, high lithium contents are predominantly observed in class I, and their interpretation is facilitated by utilizing the compositional ternary plot.

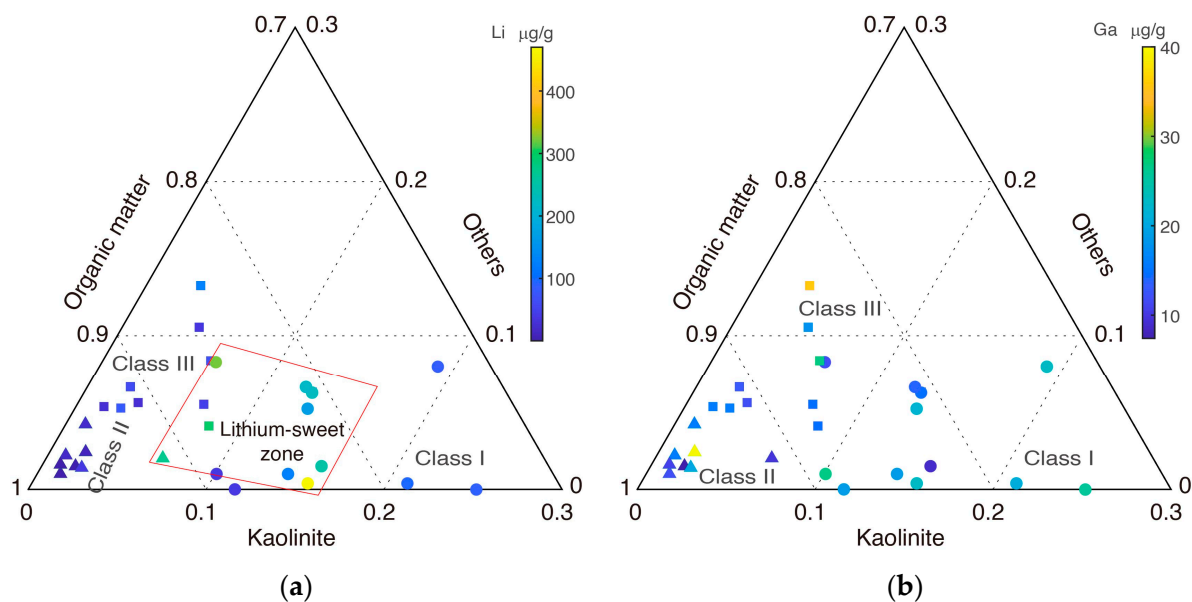


**Figure 16.** Class-related ternary plots of coal compositions after three-class classification. Circles, triangles, and rectangles represent classes I, II, and III. Colors in (a) and (b) indicate lithium and gallium contents, respectively. The dots, triangles, and rectangles represent classes I, II, and III.

### 5.2. Interpretation Method with Elasticity Cross Plot

In addition to trend fitting, this section explores the relationship between bulk modulus and modulus ratio as a means to discuss the elastic interpretation methods of gallium and lithium contents. Generally, the scatter points in Figure 17 exhibit zonal distribution characteristics under different saturation states. Specifically, under the dry state, the scatter points are concentrated in the lower half of the figure, while under the water-saturated state, they are predominantly located in the upper half. Moreover, the scatter points transition along the marked arrows when shifting from the dry to the water-saturated states, facilitating the clear differentiation between dry and water-saturated samples.

Under a given saturation state, classes I, II, and III also exhibit distinctly zonal distribution characteristics. Specifically, classes I, II, and III are situated in the up-right, bottom-left, and middle-left areas, respectively. The distribution of lithium in the plot also displays zonal characteristics akin to those observed in the compositional ternary plot, with most high-lithium samples concentrated in the marked lithium-sweet area. Because the distances among scatter points in the water-saturated state are more considerable than in the dry state, defining the lithium-sweet zone in the water-saturated state is more applicable. In contrast, the zonal distribution characteristics in the gallium figure are weak-high gallium samples which are sparsely distributed along the low modulus ratio edge, making it challenging to interpret gallium contents using the cross plot.

Like the bulk modulus vs. modulus ratio cross plot, the cross plots of shear modulus vs. modulus ratio,  $V_P$  vs. velocity ratio, and  $V_S$  vs. velocity ratio yield similar results. Using these cross plots, one can qualitatively interpret lithium-rich benches in the No. 6 coalbed. Similarly, the interpretation of gallium-rich benches in the No. 6 coalbed can be achieved by fitting the elastic parameter-gallium trend in class II, which contains the highest gallium sample.

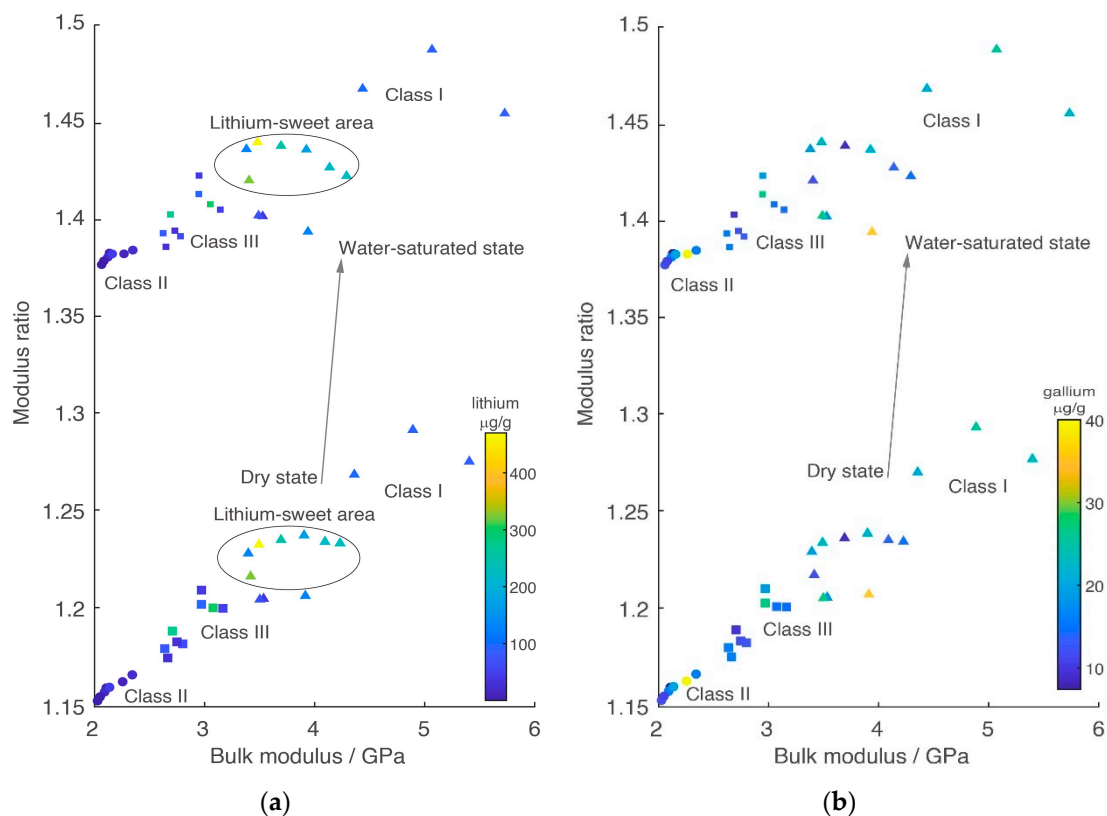


**Figure 17.** The bulk modulus vs. modulus ratio cross plots under the dry and water-saturated states for lithium (a) and gallium (b) interpretations. The triangles, dots, and rectangles represent classes I, II, and III.

## 6. Conclusions

This paper utilized the No. 6 coalbed in the Haerwusu mine as a case study to explore the zonal geochemistry and elasticity characteristics of the ultrathick gallium- and lithium-rich coalbed in North China. From the investigation, the following conclusions can be drawn:

(1) The material compositions, elastic properties, and distribution of critical metals exhibit heterogeneously within the ultrathick No. 6 coalbed, displaying distinct zonal distribution characteristics. Classifications based on coal composition notably enhance correlations among pairs such as gallium-boehmite and lithium-kaolinite. Similarly, classifications based on elastic parameters, including S-wave velocity, density, and modulus ratio, improve correlations with critical metals, namely gallium and lithium. These two classification methods yield comparable results.

(2) The host minerals for gallium and lithium in the coalbed are intricate and exhibit zonal characteristics. Within classes II and III (representing ultralow- and low-ash-yield coals), boehmite and kaolinite serve as the primary hosts for gallium and lithium, respectively. Conversely, in class I (medium-ash-yield coal), gallium is associated with kaolinite, while lithium shows low correlation coefficients with major minerals. Notably, while boehmite contents in class II are lower than in class III, individual boehmite units in class II absorb significantly more gallium than those in class III.

(3) This paper introduces a wireline-log-constrained rock physics modeling strategy aimed at bridging the mesoscale material compositions of coal with its macroscale elastic behaviors. By establishing clear correlations between host minerals and critical metals, it is possible to link the macroscale elastic responses to the microscale enrichments of gallium and lithium. This approach facilitates the exploration of interpretation methods for critical metals hosted within coal, leveraging laboratory-tested elastic responses and wireline logs.

(4) The gallium and lithium contents in the No. 6 coalbed are interpretable. Preferred methods for interpreting lithium include compositional ternary plots and elastic parameter cross plot. Similarly, preferred methods for gallium interpreting include fitting the boehmite-gallium relationship and utilizing elastic parameters.

(5) The zonal characteristics and interpretation methodologies uncovered in this study have the potential to elucidate enrichment mechanisms and advance interpretation technologies for critical metals hosted within ultrathick coalbeds.

**Author Contributions:** Conceptualization, T.C. and F.C.; methodology, T.C. and J.F.; software, T.C. and J.F.; validation, J.F.; formal analysis, T.C.; investigation, T.C. and J.F.; resources, T.C. and F.C.; data curation, J.F.; writing—original draft preparation, J.F.; writing—review and editing, T.C. and F.C.; visualization, J.F. All authors have read and agreed to the published version of the manuscript.

**Funding:** This research was funded by the National Key Research and Development Project of China, grant number 2021YFC2902003 and the Major Science and Technology Special Project of Xinjiang Uygur Autonomous Region, grant number 2022A03014.

**Data Availability Statement:** The present manuscript included all the data.

**Acknowledgments:** The authors acknowledge the anonymous reviewers for their constructive suggestions and Dai Shifeng for assisting with the geochemically measured core data in the Haerwusu mine.

**Conflicts of Interest:** The authors declare no conflicts of interest.

## Appendix A. V-R-H Average

Minerals found in coal exhibit complex compositions, geometries, and grain interactions, posing challenges for accurately estimating their effective moduli. Various estimation methods exist, with the Voigt–Reuss–Hill (V–R–H) average being a commonly employed approach in rock physics modeling. The V–R–H average is advantageous as it does not rely on specific assumptions regarding mineral geometry. In this method, the Voigt bound assumes minerals are connected in parallel [24,29], while the Reuss bound assumes they are connected in series, as expressed mathematically in Equation (A1).

$$\begin{cases} M_V = \sum_{i=1}^N f_i M_i \\ M_R^{-1} = \sum_{i=1}^N f_i / M_i \\ M_{VRH} = (M_V + M_R) / 2 \end{cases} \quad (\text{A1})$$

The equation is defined for  $N \geq 2$ , where  $f_i$  and  $M_i$  represent the volume ratio and modulus of the  $i^{\text{th}}$  mineral, respectively.  $M_R$ ,  $M_V$ , and  $M_{VRH}$  denote the effective moduli of the Reuss bound, Voigt bound, and V–R–H average. Typically, the V–R–H average provides a reasonable estimate of the effective modulus for mixtures when the minerals have similar moduli.

## Appendix B. DEM Model

The differential equivalent medium (DEM) model calculates the moduli of two-phase mixtures by incrementally introducing inclusions (phase two) into the background material (phase one). Equation (A2) represents the general mathematical expression of the model [41].

$$\begin{cases} (1-y)d[K^*(y)]/dy = (K_2 - K^*)P^{*2}(y) \\ (1-y)d[\mu^*(y)]/dy = (\mu_2 - \mu^*)Q^{*2}(y) \end{cases} \quad (\text{A2})$$

The DEM model calculates the effective bulk and shear moduli, denoted as  $K^*$  and  $\mu^*$ , respectively, by starting with the initial bulk and shear moduli of the background phase, represented by  $K^*(0) = K_1$  and  $\mu^*(0) = \mu_1$ , and then incrementally adding the bulk and shear moduli of the inclusion phase, denoted as  $K_2$  and  $\mu_2$ . Here,  $y$  represents the concentration of phase two, while  $P^{*2}$  and  $Q^{*2}$  are the geometric factors of inclusions. It is important to

note that the DEM model is a high-frequency approximation that only applies under dry conditions when dealing with pores.

### Appendix C. Gassmann Fluid Replacement

Gassmann fluid replacement is commonly employed in rock physics modeling and reservoir characterization to account for pore fluid replacement. Conventionally, its general mathematical expression is given by Equation (A3) [41].

$$\begin{cases} \frac{K_{sat1}}{K_0 - K_{sat1}} - \frac{K_{f11}}{\phi(K_0 - K_{f11})} = \frac{K_{sat2}}{K_0 - K_{sat2}} - \frac{K_{f12}}{\phi(K_0 - K_{f12})} \\ \mu_{sat1} = \mu_{sat2} \end{cases} \quad (A3)$$

where  $K_0$  is the bulk modulus of the rock matrix,  $K_{sat1}$  and  $K_{sat2}$  are the bulk moduli of the rocks saturated with fluid one and fluid two, respectively;  $\mu_{sat1}$  and  $\mu_{sat2}$  are the shear moduli of the rocks saturated with fluid one and fluid two, respectively;  $K_{f11}$  and  $K_{f12}$  are the bulk moduli of fluid one and fluid two, respectively;  $\phi$  is the porosity.

### Appendix D. Elastic Parameter Transformation

Under homogeneous, isotropic, and small-strain assumptions, the loaded stresses and observed strains correlate linearly and follow Hooke's law. Under these conditions, two out of five moduli are independent. With density, bulk modulus, and shear modulus inputs, Equation (A4) computes P- and S-wave velocities [41].

$$\begin{cases} V_P = \sqrt{(K + 4\mu/3)/\rho} \\ V_S = \sqrt{\mu/\rho} \end{cases} \quad (A4)$$

where  $K$  and  $\mu$  are bulk and shear moduli,  $\rho$  is density, and  $V_P$  and  $V_S$  are P- and S-wave velocities.

## References

- Musumeci, S.; Barba, V. Gallium Nitride Power Devices in Power Electronics Applications: State of Art and Perspectives. *Energies* **2023**, *16*, 3894. [CrossRef]
- Tabelin, C.B.; Dallas, J.; Casanova, S.; Pelech, T.; Bournival, G.; Saydam, S.; Canbulat, I. Towards a low-carbon society: A review of lithium resource availability, challenges and innovations in mining, extraction and recycling, and future perspectives. *Miner. Eng.* **2021**, *163*, 106743. [CrossRef]
- Greim, P.; Solomon, A.A.; Breyer, C. Assessment of lithium criticality in the global energy transition and addressing policy gaps in transportation. *Nat. Commun.* **2020**, *11*, 4570. [CrossRef] [PubMed]
- Dai, S.F.; Li, D.; Chou, C.L.; Zhao, L.; Zhang, Y.; Ren, D.; Ma, Y.W.; Sun, Y.Y. Mineralogy and geochemistry of boehmite-rich coals: New insights from the Haerwusu Surface Mine, Jungar Coalfield, Inner Mongolia, China. *Int. J. Coal. Geol.* **2008**, *74*, 185–202. [CrossRef]
- Hou, Y.; Dai, S.; Nechaev, V.P.; Finkelman, R.B.; Wang, H.; Zhang, S.; Di, S. Mineral matter in the Pennsylvanian coal from the Yangquan Mining District, northeastern Qinshui Basin, China: Enrichment of critical elements and a Se-Mo-Pb-Hg assemblage. *Int. J. Coal. Geol.* **2023**, *266*, 104178. [CrossRef]
- Jiu, B.; Huang, W.; Spiro, B.; Hao, R.; Mu, N.; Wen, L.; Hao, H. Distribution of Li, Ga, Nb, and REEs in coal as determined by LA-ICP-MS imaging: A case study from Jungar coalfield, Ordos Basin, China. *Int. J. Coal. Geol.* **2023**, *267*, 104184. [CrossRef]
- Liu, B.; Wang, J.; He, H.; Mishra, V.; Li, Y.; Wang, J.; Zhao, C. Geochemistry of Carboniferous coals from the Laoyaogou mine, Ningwu coalfield, Shanxi Province, northern China: Emphasis on the enrichment of valuable elements. *Fuel* **2020**, *279*, 118414. [CrossRef]
- Sun, B.L.; Zeng, F.G.; Moore, T.A.; Rodrigues, S.; Liu, C.; Wang, G.Q. Geochemistry of two high-lithium content coal seams, Shanxi Province, China. *Int. J. Coal. Geol.* **2022**, *260*, 104059. [CrossRef]
- Dai, S.F.; Jiang, Y.F.; Ward, C.R.; Gu, L.D.; Seredin, V.V.; Liu, H.D.; Zhou, D.; Wang, X.B.; Sun, Y.Z.; Zou, J.H.; et al. Mineralogical and geochemical compositions of the coal in the Guanbanwusu Mine, Inner Mongolia, China: Further evidence for the existence of an Al (Ga and REE) ore deposit in the Jungar Coalfield. *Int. J. Coal. Geol.* **2012**, *98*, 10–40. [CrossRef]
- Xie, P.; Hower, J.C.; Nechaev, V.P.; Ju, D.; Liu, X. Lithium and redox-sensitive (Ge, U, Mo, V) element mineralization in the Pennsylvanian coals from the Huangtupo coalfield, Shanxi, northern China: With emphasis on the interaction of infiltrating seawater and exfiltrating groundwater. *Fuel* **2021**, *300*, 120948. [CrossRef]

11. Dai, S.F.; Ren, D.Y.; Li, S.S. Discovery of the superlarge gallium ore deposit in Jungar, Inner Mongolia, North China. *Chin. Sci. Bull.* **2006**, *51*, 2243–2252. [[CrossRef](#)]
12. Jiu, B.; Huang, W.H.; Mu, N. Mineralogy and elemental geochemistry of Permo-Carboniferous Li-enriched coal in the southern Ordos Basin, China: Implications for modes of occurrence, controlling factors and sources of Li in coal. *Ore Geol. Rev.* **2022**, *141*, 104686. [[CrossRef](#)]
13. Horrocks, T.; Holden, E.J.; Wedge, D. Evaluation of automated lithology classification architectures using highly-sampled wireline logs for coal exploration. *Comput. Geosci.-UK* **2015**, *83*, 209–218. [[CrossRef](#)]
14. Ameen, M.S.; Smart, B.G.D.; Somerville, J.M.; Hammilton, S.; Naji, N.A. Predicting rock mechanical properties of carbonates from wireline logs (A case study: Arab-D reservoir, Ghawar field, Saudi Arabia). *Mar. Petrol. Geol.* **2009**, *26*, 430–444. [[CrossRef](#)]
15. Bai, Y.; Tan, M.J.; Shi, Y.J.; Zhang, H.T.; Li, G.R. Regression Committee Machine and Petrophysical Model Jointly Driven Parameters Prediction From Wireline Logs in Tight Sandstone Reservoirs. *IEEE Trans. Geosci. Remote Sens.* **2022**, *60*, 5900409. [[CrossRef](#)]
16. Haque, A.K.M.E.; Qadri, S.M.T.; Bhuiyan, M.A.H.; Navid, M.; Nabawy, B.S.; Hakimi, M.H.; Abd-El-Aal, A.K. Integrated wireline log and seismic attribute analysis for the reservoir evaluation: A case study of the Mount Messenger Formation in Kaimiro Field, Taranaki Basin, New Zealand. *J. Nat. Gas Sci. Eng.* **2022**, *99*, 104452. [[CrossRef](#)]
17. Shi, J.X.; Zeng, L.B.; Dong, S.Q.; Wang, J.P.; Zhang, Y.Z. Identification of coal structures using geophysical logging data in Qinshui Basin, China: Investigation by kernel Fisher discriminant analysis. *Int. J. Coal. Geol.* **2020**, *217*, 103314. [[CrossRef](#)]
18. Vallee, M.A.; Smith, R.S.; Keating, P. Metalliferous mining geophysics—State of the art after a decade in the new millennium. *Geophysics* **2011**, *76*, W31–W50. [[CrossRef](#)]
19. Dai, S.F.; Yang, J.Y.; Ward, C.R.; Hower, J.C.; Liu, H.D.; Garrison, T.M.; French, D.; O’Keefe, J.M.K. Geochemical and mineralogical evidence for a coal-hosted uranium deposit in the Yili Basin, Xinjiang, northwestern China. *Ore Geol. Rev.* **2015**, *70*, 1–30. [[CrossRef](#)]
20. Gurevich, B.; Makarynska, D.; Pervukhina, M. Ultrasonic moduli for fluid-saturated rocks: Mavko-Jizba relations rederived and generalized. *Geophysics* **2009**, *74*, N25–N30. [[CrossRef](#)]
21. Karimpouli, S.; Tahmasebi, P.; Saenger, E.H. Estimating 3D elastic moduli of rock from 2D thin-section images using differential effective medium theory. *Geophysics* **2018**, *83*, Mr211–Mr219. [[CrossRef](#)]
22. Neto, I.A.L.; Missagia, R.M.; Ceia, M.A.; Archilha, N.L.; Oliveira, L.C. Carbonate pore system evaluation using the velocity-porosity-pressure relationship, digital image analysis, and differential effective medium theory. *J. Appl. Geophys.* **2014**, *110*, 23–33. [[CrossRef](#)]
23. Zhao, L.; Chen, T.; Mukerji, T.; Zhang, M.; Xing, T. Brown and Korrington’s expression for the saturated bulk modulus at high frequencies: Modification of Mavko and Jizba’s squirt flow model. *Geophysics* **2022**, *87*, MR201–MR208. [[CrossRef](#)]
24. Chen, T.; Song, X. Are Coal-Hosted Gallium-Rich Ores Elastically Detectable: A Rock-Physics Modeling Perspective. *Minerals* **2022**, *12*, 1619. [[CrossRef](#)]
25. Gang, X.; Tingting, M.; Chaofeng, W.; Hongwei, J.; Yunlong, W. Study on the Characteristics of Coal Ultrasonic Response during Loading and Its Influence Mechanism. *Sustainability* **2023**, *15*, 1093. [[CrossRef](#)]
26. Zhao, T.; Zou, G.; Peng, S.; Zeng, H.; Gong, F.; Yin, Y. Analysis of the viscoelasticity in coal based on the fractal theory. *Geophysics* **2022**, *88*, WA177–WA187. [[CrossRef](#)]
27. Zou, G.G.; Zeng, H.; Peng, S.P.; Zhou, X.Y.; Satibekova, S. Bulk density and bulk modulus of adsorbed coalbed methane. *Geophysics* **2019**, *84*, K11–K21. [[CrossRef](#)]
28. Ba, J.; Cao, H.; Carcione, J.M.; Tang, G.; Yan, X.F.; Sun, W.T.; Nie, J.X. Multiscale rock-physics templates for gas detection in carbonate reservoirs. *J. Appl. Geophys.* **2013**, *93*, 77–82. [[CrossRef](#)]
29. Ba, J.; Hu, P.; Tan, W.H.; Muller, T.M.; Fu, L.Y. Brittle mineral prediction based on rock-physics modelling for tight oil reservoir rocks. *J. Geophys. Eng.* **2021**, *18*, 970–983. [[CrossRef](#)]
30. Pan, X.P.; Zhang, G.Z.; Chen, J.J. The construction of shale rock physics model and brittleness prediction for high-porosity shale gas-bearing reservoir. *Petrol. Sci.* **2020**, *17*, 658–670. [[CrossRef](#)]
31. Finkelman, R.B.; Palmer, C.A.; Wang, P. Quantification of the modes of occurrence of 42 elements in coal. *Int. J. Coal. Geol.* **2018**, *185*, 138–160. [[CrossRef](#)]
32. Wedepohl, K.H. *Handbook of Geochemistry*; Springer: Heidelberg, Germany, 1969.
33. Fairén, A.G.; Losa-Adams, E.; Gil-Lozano, C.; Gago-Duport, L.; Uceda, E.R.; Squyres, S.W.; Rodríguez, J.A.P.; Davila, A.F.; McKay, C.P. Tracking the weathering of basalts on Mars using lithium isotope fractionation models. *Geochem. Geophys. Geosyst.* **2015**, *16*, 1172–1197. [[CrossRef](#)] [[PubMed](#)]
34. Li, W.; Liu, X.-M. Experimental investigation of lithium isotope fractionation during kaolinite adsorption: Implications for chemical weathering. *Geochim. Cosmochim. Acta* **2020**, *284*, 156–172. [[CrossRef](#)]
35. Li, W.; Chen, T.; Song, X.; Gong, T.; Liu, M. Reconstruction of critical coalbed methane logs with principal component regression model: A case study. *Energ. Explor. Exploit.* **2020**, *38*, 1178–1193. [[CrossRef](#)]
36. Kanungo, T.; Mount, D.M.; Netanyahu, N.S.; Piatko, C.D.; Silverman, R.; Wu, A.Y. An efficient k-means clustering algorithm: Analysis and implementation. *IEEE Trans. Pattern Anal. Mach. Intell.* **2002**, *24*, 881–892. [[CrossRef](#)]
37. Dai, S.F.; Hower, J.C.; Finkelman, R.B.; Graham, I.T.; French, D.; Ward, C.R.; Eskenazy, G.; Wei, Q.; Zhao, L. Organic associations of non-mineral elements in coal: A review. *Int. J. Coal. Geol.* **2020**, *218*, 103347. [[CrossRef](#)]

38. Geboy, N.J.; Engle, M.A.; Hower, J.C. Whole-coal versus ash basis in coal geochemistry: A mathematical approach to consistent interpretations. *Int. J. Coal. Geol.* **2013**, *113*, 41–49. [[CrossRef](#)]
39. Jiu, B.; Jin, Z.; Wang, Z. Multiscale in-situ elemental characterization of critical elements in low rank coal, implications for modes of occurrence. *Fuel* **2023**, *349*, 128632. [[CrossRef](#)]
40. Cosenza, P.; Giot, R.; Hedan, S. Elastic moduli of clay minerals and their aggregates: A review. *Appl. Clay Sci.* **2023**, *236*, 106878. [[CrossRef](#)]
41. Mavko, G.; Mukerji, T.; Dvorkin, J. *The Rock Physics Handbook*; Cambridge University Press: Cambridge, UK, 2020; pp. 613–672.
42. Cui, C.; Chang, S.L.; Yao, Y.B.; Cao, L.T. Quantify Coal Macrolithotypes of a Whole Coal Seam: A Method Combining Multiple Geophysical Logging and Principal Component Analysis. *Energies* **2021**, *14*, 213. [[CrossRef](#)]

**Disclaimer/Publisher’s Note:** The statements, opinions and data contained in all publications are solely those of the individual author(s) and contributor(s) and not of MDPI and/or the editor(s). MDPI and/or the editor(s) disclaim responsibility for any injury to people or property resulting from any ideas, methods, instructions or products referred to in the content.